THE JOURNAL OF PHYSICAL CHEMISTRY B

pubs.acs.org/JPCB Article

Development of Cu^{2+}-Based Distance Methods and Force Field Parameters for the Determination of PNA Conformations and Dynamics by EPR and MD Simulations

Austin Gamble Jarvi, Artur Sargun, Xiaowei Bogetti, Junmei Wang,* Catalina Achim,* and Sunil Saxena*

Cite This: https://dx.doi.org/10.1021/acs.jpcb.0c05509 Read Online

ACCESS | Metrics & More | Article Recommendations | Supporting Information

ABSTRACT: Peptide nucleic acids (PNAs) are a promising group of synthetic analogues of DNA and RNA that offer several distinct advantages over the naturally occurring nucleic acids for applications in biosensing, drug delivery, and nanoelectronics. Because of its structural differences from DNA/RNA, methods to analyze and assess the structure, conformations, and dynamics are needed. In this work, we develop synergistic techniques for the study of the PNA conformation. We use CuQ_2, a Cu^{2+} complex with 8-hydroxyquinoline (HQ), as an alternative base pair and as a spin label in electron paramagnetic resonance (EPR) distance methods. We use molecular dynamics (MD) simulations with newly developed force field parameters for the spin labels to interpret the distance constraints determined by EPR. We complement these methods by UV−vis and circular dichroism measurements and assess the efficacy of the Cu^{2+} label on a PNA duplex whose backbone is based on aminoethylglycine and a duplex with a hydroxymethyl backbone modification. We show that the Cu^{2+} label functions efficiently within the standard PNA and the hydroxymethyl-modified PNA and that the MD parameters may be used to accurately reproduce our EPR findings. Through the combination of EPR and MD, we gain new insights into the PNA structure and conformations as well as into the mechanism of orientational selectivity in Cu^{2+} EPR at X-band. These results present for the first time a rigid Cu^{2+} spin label used for EPR distance measurements in PNA and the accompanying MD force fields for the spin label. Our studies also reveal that the spin labels have a low impact on the structure of the PNA duplexes. The combined MD and EPR approach represents an important new tool for the characterization of the PNA duplex structure and provides valuable information to aid in the rational application of PNA at large.

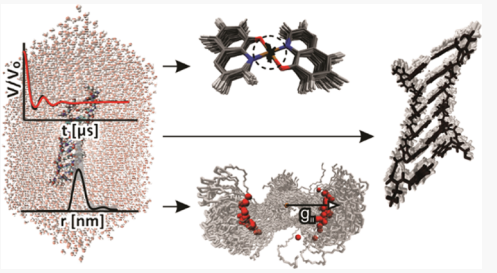

INTRODUCTION

Nucleic acids are an incredibly versatile category of macromolecules that have wide-ranging applications. These molecules have been used to create nanostructures and nanoarchitectures,[1−3] molecular machines,[4−6] biological sensors,[7−9] and drug delivery systems[10−12] and in the design of therapeutic methods.[13,14] Much of this field is dominated by DNA, but in recent years, synthetic nucleic acids with favorable properties have also gained prominence.[15,16]

One of these synthetic nucleic acids is peptide nucleic acid (PNA).[17] The PNA backbone is based on aminoethylglycine (aeg) instead of the sugar-diphosphate found in DNA/RNA (Figure S1). Complementary strands of PNA engage in the Watson−Crick base pairing to form double helix structures.[18,19] PNA has several properties distinct from DNA and RNA that can be exploited in fundamental and practical applications. The pseudopeptide backbone of PNA lacks the negatively charged diphosphate group found in traditional nucleic acids. Consequently, there are no repulsive electrostatic forces between complementary PNA strands in a duplex and a PNA duplex is more stable than a DNA duplex with the same sequence of nucleobases.[20,21] Additionally, the aeg backbone is not recognized by enzymes, which makes PNA resistant to enzymatic degradation, a useful trait for biological applications.[22] Modification of the PNA monomers with various substituent groups to tailor the functionality of a PNA duplex is also relatively simple compared to the modification of DNA or RNA.[23]

These characteristics make PNA a promising material for nanotechnological applications.[24,25] In particular, PNA has the potential as a tool for nanoassemblies and as a material for nanoelectronics.[26,27] In both applications, it is important to understand the structure and dynamics of the material to gain greater control over the desired architecture of the nanostructures.[28] Such control increases the chances that complex nanostructures can be built and enhances the ability to tailor the nanostructures to specific applications. In the context of nanoelectronics, it has been shown that the structure and dynamics of the PNA duplex have a significant impact on

Received: June 17, 2020
Revised: July 14, 2020
Published: August 11, 2020

its charge-transfer properties.[29−31] Clearly, a thorough understanding of the structure and dynamics of PNA is paramount to expanding its application. While methods such as NMR and X-ray crystallography enable the determination of a PNA structure, these methods can suffer from complications such as the requirement for crystallization or from size limitations.[32−34] To this end, we show that electron paramagnetic resonance (EPR) combined with molecular dynamics (MD) is a robust technique to assess the PNA structure.

EPR, and particularly EPR-based nanoscale distance measurements, is a powerful technique to measure the structure and conformational dynamics of a wide variety of macromolecules.[35−43] Because EPR detects species with unpaired electrons, it is necessary to site-selectively incorporate EPR-active species within the macromolecule.[44] These species are often organic radicals[45,46] or paramagnetic metal ions.[47−67] To date, much work has been performed to develop EPR-active labels for DNA and RNA to measure their structure and dynamics.[68−70] Some nitroxide spin labels have been developed for use with PNA, but these are limited to peptide conjugates of PNA[71] or are restricted to attachment at the N-terminus.[72,73] In this work, we present a spin label for use with EPR distance measurements that uses two 8-hydroxyquinoline (HQ) moieties positioned complementarily within the PNA duplex that rigidly coordinate a Cu^{2+} ion. This spin labeling scheme is advantageous in that the rigidity allows for precise conformational determination of the PNA, as well as the fact that this label can be positioned anywhere inside the PNA duplex.

We also have developed MD force field parameters for the spin label to be used in conjunction with EPR distance measurements. Because the EPR method provides sparse constraints, additional techniques are often used for the interpretation of the measured distances in terms of structure and dynamics. In particular, MD simulations have achieved great success in interpreting EPR distance constraints with regard to molecular conformations.[74−80] MD on PNA systems using CHARMM-,[81,82] GROMACS-,[83] and AMBER-based[84,85] force fields has yielded useful insights.[85] However, the current PNA force fields do not include parameters for EPR spin labels that can provide further structural and dynamical insight and context. Herein, we developed such force field parameters to enable maximally accurate MD simulations.

Using EPR methods and MD simulations together, we examine a standard PNA duplex, i.e., a PNA whose backbone is aeg and a PNA duplex that has a hydroxymethyl group in the γ position of aeg. Through both methods, we analyze the conformation of the PNA duplexes and gain physical insight into the experimental EPR methodology used to measure distances.

METHODS

EPR Measurements. Continuous wave (CW) EPR measurements were performed on a Bruker Elexsys E580 CW/FT X-band spectrometer using a Bruker ER4118X-MD5 resonator at 80 K. The CW EPR experiments were run with a center field of 3100 G and a sweep width of 2000 G, a modulation amplitude of 4 G, and a modulation frequency of 100 kHz for 1024 data points using a conversion time of 20.48 ms. CW EPR for unmodified (U)-PNA was performed at 9.680015 GHz. CW EPR for γ-PNA was performed at 9.68077 GHz. CW EPR was performed at multiple microwave powers to exclude saturation effects (see Figure S2). CW EPR simulations were performed with EasySpin.[86]

The Cu^{2+} concentration was measured using a calibration curve of EPR samples of $CuSO_4$ in water with 25% v/v glycerol at Cu^{2+} concentrations of 50, 75, 100, 150, 200, 400, 600, 800, 1000, 1500, and 2000 μM. CW EPR spectra were obtained using the same experimental parameters listed above. Double-integrated intensities for the standard calibration samples and the Cu^{2+}-containing PNA samples were calculated using Xepr.

Four-pulse double electron−electron resonance (DEER) measurements were performed on a Bruker Elexsys E680 CW/FT X-band spectrometer using a Bruker EN4118X-MD4 resonator at 20 K. Temperature was controlled by an Oxford ITC503 temperature controller and an Oxford CF935 dynamic continuous flow cryostat connected to an Oxford LLT 650 low-loss transfer tube. The pulse sequence was $(\pi/2)_{\nu 1}-\tau_1-(\pi)_{\nu 1}-\tau_1 + t-(\pi)_{\nu 2}-\tau_2-$t-$(\pi)_{\nu 1}-\tau_2-$echo. The observer $(\pi/2)_{\nu 1}$ and $(\pi)_{\nu 1}$ pulses were 16 and 32 ns, respectively. The pump $(\pi)_{\nu 2}$ pulse was 16 ns. The time t was increased by a step size of 12 ns over 128 points. The time domain data was analyzed by Tikhonov regularization.[87] Data acquisition lasted approximately 12−24 h. DEER data was processed using DeerAnalysis2018.[88]

EPR Sample Preparation. Fifty to hundred micromolar solutions of the PNA duplexes in pH 7.0 of 10 mM sodium phosphate buffer were annealed in the presence of 2 equiv of Cu^{2+} by slow cooling from 95 °C to room temperature over 2−3 h. Twenty-five percent of glycerol (v/v) was added as a glassing agent after annealing.

Force Field Parameterization. We performed force field parameterization for 10 PNA residues following the standard AMBER force field development procedure. We parameterized 10 total PNA residues, adenine, cytosine, guanine, and thymine on the standard aeg backbone (APN, CPN, GPN, and TPN, respectively), and also the same residues with a backbone modified by a hydroxymethyl group attached to the methylene group next to the N-terminus (γ-modification) (APR, CPR, GPR, and TPR, respectively), as well as two 8-hydroxyquinoline PNA residues (QPC and QPN) and the Cu^{2+} ion (Cu). Two designations were used for HQ residues (QPC/QPN) in the pair of complementary ligands because the equilibrium bond angles between Cu^{2+} and the coordinating oxygens and nitrogens are slightly asymmetric between the two HQ ligands. This asymmetry is likely because one of the HQ groups is closer to the N-end of its strand, while the other ligand is closer to the C-end of its strand. Therefore, within the QPN residue, the coordinating oxygen and nitrogen atoms required atom-type designations different from those in QPC to ensure proper geometry. The chemical structures of these residues are shown in Figure S1. For each residue, we constructed a model compound by adding an acetyl (ACE) group to N-terminus and an *N*-methyl amide (NME) group to C-terminus. These additions make the PNA monomers for which the force field development is performed more similar to that of the PNA monomers in the PNA oligomer.

We conducted ab initio calculations for the model compounds using the Gaussian 16 software package.[89] We used the B3LYP/6-311++G(d,p) optimization followed by single-point electrostatic potential (ESP) calculation at the HF/6-31G* level. The ab initio ESP was used to derive point charges with the RESP program.[90] For the QPC/QPN model compound, the solvent effect was taken into account in the optimization step by using the polarizable continuum model

https://dx.doi.org/10.1021/acs.jpcb.0c05509
J. Phys. Chem. B XXXX, XXX, XXX−XXX

Table 1. Molecular Weights and MALDI-ToF MS Data for the PNA Oligomers[a]

PNA name	PNA sequence	calculated	exp.
U-PNA	H_2N-^{L}Lys-GTQCATCQAG-H	2905.6 ($M + Na^+$)	2906.35
	H-CAQGTAGQTC-^{L}Lys-NH_2		2907.18
γ-PNA	H_2N-^{L}Lys-GTQC$^{\gamma}$AT$^{\gamma}$CQAG-H	2965.7 ($M + Na^+$)	2961.2
	H-CAQG$^{\gamma}$TA$^{\gamma}$GQTC-^{L}Lys-NH_2		2964.5

[a]^{L}Lys = L-lysine, Q = 8-hydoxyquinoline PNA monomer, and γ = hydroxymethyl backbone modification.

(PCM) implemented in Gaussian 16. Frequency analysis was also conducted for the model compound to derive force field parameters for bonds involving Cu^{2+}. We used the Residuegen program in the Antechamber module[91] to generate the topology of the A, G, C, and T PNA monomers; the program removes the capping atoms and adds a charge group constraint (the net charge of the capping groups is zero) during the RESP charge fittings. For the CuQ_2 complex within the PNA, QPC−Cu−QPN, we first derived charges with all four capping residues removed using the Residuegen program. We found that the partial charge of the Cu atom is 1.015. For the sake of simplicity, we made the point charge of Cu^{2+} 1.0 so that QPC and QPN residues each bore a −0.5 net charge. We then derived the partial charges of the QPC/QPN residues using the Residuegen program, keeping only one residue (either QPC or QPN), as partial charges of the corresponding atoms between the two residues are the same. This treatment is reasonable as the ESP relative RRMS value, which measures the charge fitting performance, is essentially the same for the Residuegen runs of the QPC−Cu−QPN complex and the individual QPC/QPN residues. Note that RRMS is the square root of the ratio between the residual sum of ESP squares after fitting and the initial sum of ESP squares.

We assigned atom types using the definition table for AMBER biomolecular force fields, Parm10.[92] The missing force field parameters came from either Parm10 or the general AMBER force field (GAFF),[93] in the case that the force field parameter substitutions using Parm10 were not successful. For the force field parameters involving Cu^{2+}, the van der Waals parameters were calculated using the ionization potential and atomic polarizability of Cu^{2+}, as detailed in our previous publication.[94] The bond length and bond angle parameters were obtained by analyzing the B3LYP/6-311++G(d,p)-optimized geometry of the model compound. The bond stretching and bond angle bending force constants were calculated using empirical equations with parameters derived to reproduce the ab initio vibrational frequencies.[94] Finally, the torsional angle force constant was set to 0.0 when Cu^{2+} was not an ending atom, whereas it adopted a value of the corresponding generic torsional angle in Parm10 or GAFF. The residue topologies and the force field parameters for the 10 PNA residues are provided at the end of the Supporting Information.

Molecular Dynamics Simulations. All systems were simulated using AMBER16.[95] The ff14SB AMBER force field was used for the lysine residues. Solvent waters were treated with the TIP3P water model.[96] The PNA duplexes were solvated in a water box with dimensions 1.5 nm greater than the outermost dimensions of the PNA in the *X*, *Y*, and *Z* directions. Twenty Na^+ and Cl^- ions each were added to the water box to neutralize the system and maintain the ionic strength of the simulation system. All simulations were performed using the pmemd program in the AMBER16 software package. The ionized and solvated systems were energy-minimized with a harmonic restraint force constant that was gradually reduced from 20, 10, 5, 1 to 0 kcal/(mol Å^2). Each system was then gradually heated from 0 to 298.15 K. The temperature was maintained at 298.15 K for the full simulation. Periodic boundary conditions along with particle mesh Ewald (PME) were applied to accurately account for long-range electrostatic interactions. The temperature was controlled with the Langevin thermostat using a collision frequency of 5.0 ps^{-1}. The targeted pressure was set to 1 atm with a relaxation time of 1.0 ps. The integration time step was set to 2 ps for the equilibrium and sample phases. After the system reached equilibrium around 1 ns, MD snapshots were collected every 10 ps for 100 ns. The postanalysis and *g*-tensor calculations with ORCA were conducted on the MD snapshots.[97,98] All molecular visualization was done using visual molecular dynamics (VMD).[99]

Solid-Phase PNA Synthesis. PNA oligomers were prepared by solid-phase peptide synthesis on a 4-methylbenzhydrylamine hydrochloride (MBHA) resin downloaded with L-Lys to a 0.1 mequiv/g NH_2 content.[100] Boc/Z-protected PNA monomers were purchased from PolyOrg Inc. and used without further purification. 8-Hydroxyquinoline-modified PNA monomers were synthesized as previously described.[101] The PNA oligomers were cleaved from the solid support using a mixture of *m*-cresol/thioanisole/trifluoromethanesulfonic acid (TFMSA)/trifluoroacetic acid (TFA) (1:1:2:6) for 1 h. Cleaved PNA was precipitated using diethyl ether and purified by reversed-phase high-performance liquid chromatography (HPLC) using a C_{18} silica column on a Waters 600 controller and pump. Absorbance was measured with a Waters 2996 photodiode array detector. Characterization of the oligomers was done by matrix-assisted laser desorption ionization time-of-flight (MALDI-ToF) mass spectrometry (MS) on an α-cyano-4-hydroxycinnamic acid matrix (10 mg/mL in 1:1 water/acetonitrile, 0.1% TFA). The experimental molecular weights of the synthesized PNA oligomers are reported in Table 1.

Circular Dichroism (CD) Spectroscopy. Circular dichroism (CD) spectra were measured for 5 μM PNA solutions in pH 7.0 of 10 mM sodium phosphate buffer on a JASCO J-715 spectropolarimeter equipped with a thermoelectrically controlled, single cell holder. CD spectra were collected at 20 °C, using 1 nm bandwidth, 1 s response time, 50 nm/min speed, 20 mdeg sensitivity, and 10 scan accumulation.

UV−Vis Spectroscopy. UV−vis experiments were performed on a Varian Cary 3 spectrophotometer equipped with a programmable temperature block, in quartz cells of 10 mm optical path. PNA stock solutions were prepared in nanopure water (18.2 MΩ·cm). PNA concentrations were determined by UV−vis spectrophotometry, assuming ε(260 nm) = 8600, 6600, 13 700, and 11700 cm^{-1}·M^{-1} for the T, C, A, and G monomers, respectively, and ε(260 nm) = 2574 cm^{-1}·M^{-1} for the Q monomer.[101,102] PNA solutions for melting curves and

https://dx.doi.org/10.1021/acs.jpcb.0c05509
J. Phys. Chem. B XXXX, XXX, XXX−XXX

titration had concentrations in the 5−10 μM range and were prepared in pH 7.0 of 10 mM sodium phosphate buffer.

UV melting curves were recorded in the 5−90 °C temperature range at the rate of 1 °C/min. The melting curves were measured at the maximum absorbance of PNA, which is 260 nm. Prior to the measurement of the melting profiles, the solutions were kept at 95 °C for 10 min. T_m is the maximum of the first derivative of the melting curve.

UV−vis titrations were carried out by the addition of aliquots of standard 1000 μM $CuCl_2$ aqueous solutions to 10 μM PNA duplex solutions in pH 7.0 of 10 mM sodium phosphate buffer. The absorbance, A, was corrected (A_{corr}) for dilution.

RESULTS AND DISCUSSION

To assess the EPR distance methods, we studied two PNA duplexes with 10 base pairs whose sequences are shown in Figure 1B,C. The duplex U-PNA had a backbone based on aeg

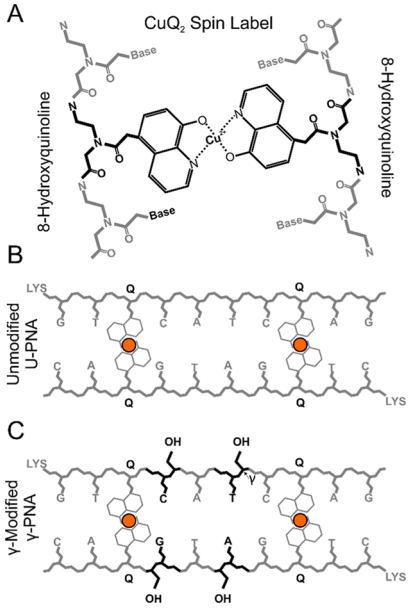

Figure 1. (A) Schematic structure of the CuQ_2 sites in the unmodified, aeg PNA (U-PNA). (B) Schematic representation of the unmodified PNA duplex; and (C) schematic representation of the γ-hydroxymethyl-modified PNA duplex (γ-PNA). Full chemical structures are included in Figure S3.

(Figure 1A,B); the γ-PNA duplex had two monomers with a γ-modified backbone at positions 4 and 6 (Figure 1C). In previous work, similar γ modifications showed a rigidifying effect on the PNA.[31,34,103,104] An L-lysine amino acid was included at the C-terminus of each PNA strand to increase the solubility of the PNA duplex. This terminal amino acid also induces a preferred handedness in the duplex.[105] Two pairs of 8-hydroxyquinoline (HQ)-modified PNA monomers were incorporated in the 10-base pair PNA duplex at positions 3 and 8 (Figure 1B,C). The two HQ groups in each pair of ligands coordinate a Cu^{2+} ion to form a bis-ligand CuQ_2 complex (Figure 1A) that acts as spin label. The full chemical structures of each PNA are included in Figure S3. The distance distribution between the two-spin labels in each duplex may be measured by EPR. The analysis of these distances by MD simulations can provide information on the accessible conformations of the PNA duplexes.

Characterization of Cu^{2+} Binding in the CuQ_2 Complex. We characterized the U-PNA to ensure that the Cu^{2+} was binding to form the CuQ_2 motif and that the loading efficiency of these sites was sufficient to perform EPR distance measurements on the U-PNA system. We performed continuous wave (CW) EPR (Figure 2A) at X-band (ca. 9.5 GHz). The CW EPR spectrum is sensitive to the coordination of the Cu^{2+} ion and informs us on the amount of Cu^{2+} bound to the HQ sites. Figure 2A shows the CW EPR spectrum obtained using a 2:1 ratio of Cu^{2+} to PNA. The spectrum (black line in Figure 2A) was simulated as a superposition (red line) of two spectral components shown as blue dashed and pink dotted lines below the measured spectrum. These two components are attributed to Cu^{2+} in two distinct coordination environments. The concentration of Cu^{2+} was determined from the double-integrated intensity of the CW EPR spectrum and agreed with the expected amount of Cu^{2+} based on sample preparation to within 5%. We therefore assume that the CW EPR spectrum represents all Cu^{2+} added to the system. The majority component, shown in blue dashed lines, exhibited EPR parameters of $g_\perp$ = 2.0418, $g_\parallel$ = 2.2190, $A_\perp$ = 25 G (71 MHz), and $A_\parallel$ = 197 G (563 MHz). These parameters agree with literature values for the CuQ_2 groups within the PNA[101] and are indicative of a square planar coordination environment of two oxygen and two nitrogen atoms.[106] The sharp features around ∼3400 G in the CW spectrum are due to super-hyperfine interactions from the two coordinating nitrogen nuclei. The simulations indicate that the fraction of spins in a CuQ_2 site, F_{CuQ_2}, is 86 ± 5%.

The EPR parameters for the second component, shown in pink dotted lines, are $g_\perp$ = 2.0603, $g_\parallel$ = 2.2404, $A_\perp$ = 10 G (29 MHz), and $A_\parallel$ = 174 G (546 MHz). These parameters are different from those of Cu^{2+} complexes in the same buffer used to dissolve the PNA duplexes (Figure S4), indicating that this component is not due to free Cu^{2+} in solution. The $g_\parallel$ of the second component is larger and the $A_\parallel$ is smaller compared to the values of the main CuQ_2 component but are still indicative of a square planar or axial coordination geometry. This component could be due to the coordination of one HQ ligand and adjacent nucleobases, backbone amide, water, or buffer molecules.[107]

We also characterized the geometry of the CuQ_2 complex in silico to ensure that the CuQ_2 in the context of the PNA residue is comparable to the established crystal structures and to inform our interpretation of our experimental results. The geometry of the CuQ_2 complex was optimized via quantum mechanical calculations (see the Methods section). The optimized geometry of the CuQ_2 complex is shown in Figure 2B in a top-down and profile view. This optimized structure is generally consistent with crystal structures of CuQ_2 groups, with the Cu^{2+} coordinated by two oxygen and two nitrogen atoms.[108,109] However, the angle between the normal of the planes of each HQ moiety is ∼25°. In crystal structures of the CuQ_2 complex, the HQ rings are coplanar.[108,109] The difference in geometry between the optimized structure and the crystal structure may be due to the lack of constraining crystal lattice, the steric effect exerted by the PNA backbone on the complex, or due to limitations of the basis sets used in quantum mechanical calculations.

UV−Vis Spectroscopy Results Support CW EPR Results. The Cu^{2+} binding to the ligands in the PNA duplexes was also measured by UV−vis titrations (Figures S5 and 2C).

https://dx.doi.org/10.1021/acs.jpcb.0c05509
J. Phys. Chem. B XXXX, XXX, XXX−XXX

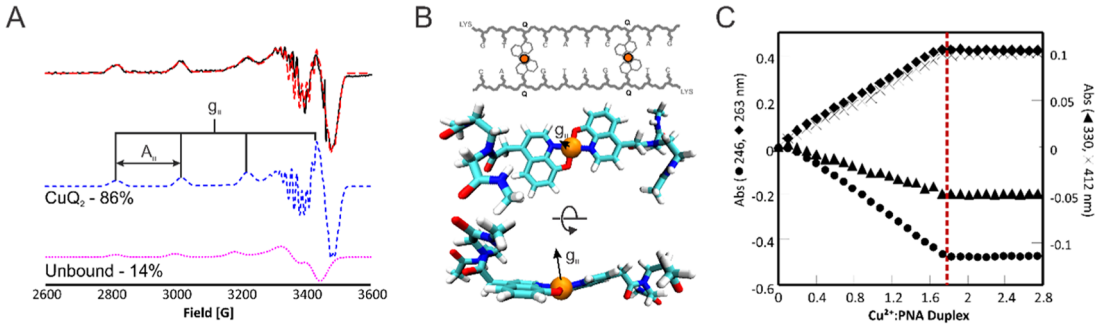

Figure 2. (A) X-band CW EPR spectrum of U-PNA (black line). The simulations of spectral components attributed to CuQ_2 sites and to nonspecifically bound Cu^{2+} are shown in blue dashed and pink dotted lines, respectively, below the experimental spectrum. The $g_{\parallel}$ (2.2190) and $A_{\parallel}$ (197 G, 563 MHz) parameters are marked in the CuQ_2 spectrum. The sum of the two components is shown as a red dashed line overlaid with the experimental data. (B) Geometry-optimized structure of the CuQ_2 binding motif using the B3LYP/6-311++G(d,p) model. The Cu^{2+} center is shown as an orange sphere, and the direction of the $g_{\parallel}$ axis is shown. (C) UV−vis titration curves for the U-PNA duplex with Cu^{2+}. The absorbance was measured at four wavelengths: 246 (circles), 263 (rhombus), 330 (triangles), and 412 nm (crosses).

The absorbance at 246, 263, and 330 nm corresponds to $\pi-\pi^*$ transitions of the HQ ligand; the absorbance at 412 nm is due to a metal-to-ligand charge-transfer band.[101] These transitions are sensitive to the binding of Cu^{2+} to the HQ ligands (Figure S5). Figure 2C shows the titration curves, i.e., the changes in absorbance at the four wavelengths mentioned above as a function of Cu^{2+}/U-PNA-duplex ratio. These curves show an inflection point at a ratio of Cu^{2+}/U-PNA duplex of 1.8:1, which corresponds to 90% Cu^{2+} being bound to the Q ligands in the U-PNA duplexes and agrees well with the CW EPR result.

DEER Measurements. We performed double electron−electron resonance (DEER) distance measurements on the U-PNA at X-band frequencies (ca. 9.5 GHz) (Figure 3).[39,40] The analysis of DEER data provides information on the probability distribution of distances between Cu^{2+} sites as well as the Cu^{2+} loading. The DEER data was collected at two magnetic fields corresponding to $g_{\perp}$ (Figure 3A,B) and $g_{\parallel}$ (Figure 3C,D) to probe this system for orientational selectivity. Orientational selectivity is a phenomenon in which DEER measurements at different magnetic fields result in different experimental signals. Such effects can occur when only a small fraction of the total EPR spectrum is excited during DEER, which may lead to only a small fraction of molecular orientations being selected.[110−122] For our system, the DEER measurements at the two different fields produced a similar dipolar modulation frequency and distance distribution. The agreement between the two magnetic fields indicates that this system is not orientationally selective at X-band. This observation is discussed in detail later.

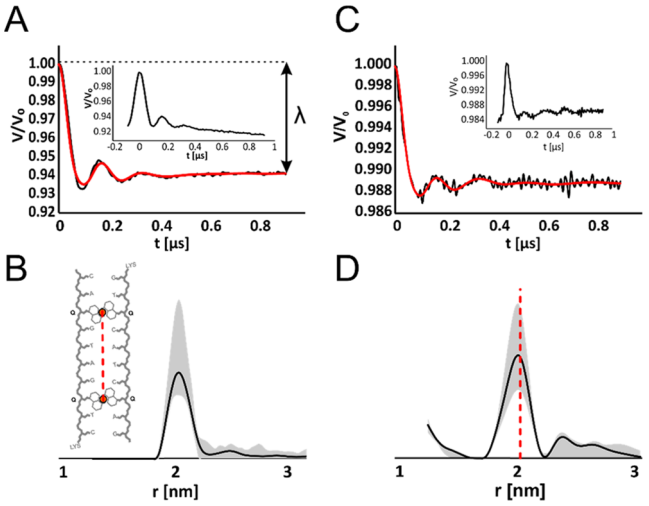

Figure 3. (A) Background-subtracted DEER signal (black line) with Tikhonov-regularized fit (red line) and raw time domain (inset) measured at $g_{\perp}$. λ is the modulation depth parameter. (B) Tikhonov-regularized DEER distance distribution at $g_{\perp}$ of U-PNA (the duplex is shown in the inset). The gray shading indicates the uncertainty of the distance measurement. (C) Background-subtracted DEER signal (black line) with Tikhonov-regularized fit (red line) and raw time domain (inset) measured at $g_{\parallel}$. (D) Tikhonov-regularized DEER distance distribution at $g_{\parallel}$. The red dashed line indicates the most probable distance from the $g_{\perp}$ distance distribution from (B).

We observed a single narrow distance distribution centered at 2.0 nm (Figure 3B,D). The standard deviation (s.d.) of the distribution (full width at half-maximum (FWHM)) is ∼0.2 nm, which indicates a small range of accessible conformations. This distribution width is similar in magnitude to that observed for comparable DNA duplexes labeled with rigid nitroxide.[123]

Estimates of Loading Efficiency from DEER. In addition to distance constraints, DEER can provide insight into the loading efficiency of the CuQ_2 sites. While our CW data provides the fraction of Cu^{2+} spins in the bound and unbound states, analysis of DEER can inform us on the fraction of PNA duplexes that have two loaded CuQ_2 sites and those that have only one loaded CuQ_2. Such information is determined through the analysis of the modulation depth parameter, λ (Figure 3A), which depends in part on the number of coupled spins in the various species present in solution. The value of λ is easily read off from our experimental DEER data (λ = 0.059 ± 0.003).

The U-PNA system has a maximum of two coupled spins—one Cu^{2+} in each CuQ_2 binding site in the PNA duplex. In a two-spin system, the modulation depth is defined as[52,53]

$$\lambda = 1 - [f_2(1 - p_b) + f_1 + f_N] \quad (1)$$

where f_2 is the fraction of species attributed to PNA duplexes that contain two loaded CuQ_2 sites, f_1 is the fraction of species attributed to PNA duplexes that have only one loaded CuQ_2, and f_N is the fraction of species containing only one Cu^{2+} (but not bound to HQ in the PNA duplex). For simplicity, we assume that nonspecifically bound Cu^{2+} ions are not interacting with PNA duplexes that contain loaded CuQ_2 groups. Additionally

https://dx.doi.org/10.1021/acs.jpcb.0c05509
J. Phys. Chem. B XXXX, XXX, XXX−XXX

$$f_2 + f_1 + f_N = 1 \quad (2)$$

In eq 1, p_b is the probability that a "B" spin will be excited in DEER and its value can be calculated from the echo-detected, field-swept EPR spectrum.[124] The probability, p_b, is calculated as the percentage of the area of the EPR spectrum that is excited by the pump pulse. The value of p_b is dependent on both the experimental parameters that dictate the pump pulse characteristics and the experimental EPR spectrum for a given sample, and therefore, p_b is unique for every system and experiment.

The DEER species fractions from eq 1 may be related to the component ratio observed in the CW EPR data (cf. Figure 2)

$$F_{CuQ_2} = \frac{2f_2 + f_1}{2f_2 + f_1 + f_N} \quad (3)$$

$$F_{Nonspecific} = \frac{f_N}{2f_2 + f_1 + f_N} \quad (4)$$

where F_{CuQ_2} is the fraction of spins in a CuQ_2 site and $F_{Nonspecific}$ is the fraction of nonspecifically bound spins. Both F_{CuQ_2} and $F_{Nonspecific}$ are readily available from the CW simulations (Figure 2). Specifically, $F_{CuQ_2} = 0.86$ and $F_{Nonspecific} = 0.14$. It is important to note that the fractions, F_{CuQ_2} and $F_{Nonspecific}$, are proportional to the concentrations of the CuQ_2 and nonspecifically bound species, respectively. The DEER modulation depth, on the other hand, does not directly reflect the species concentration, but is instead sensitive to the number of coupled spin species and uncoupled spin species, as per eq 1. Therefore, every doubly labeled PNA that contributes one unit to f_2 will contribute two units to F_{CuQ_2}, because a single coupled spin species contains two Cu^{2+} centers. This important distinction means that $F_{CuQ_2} \neq f_2 + f_1$ and $F_{Nonspecific} \neq f_N$.

Using the constraints of eqs 1−4, we can calculate a species distribution for samples of U-PNA that contain Cu^{2+}. Doing so, we arrive at $f_2 = 0.78 \pm 0.03$, $f_1 = 0.03 \pm 0.03$, and $f_N = 0.19 \pm 0.04$. The errors in the fractions were calculated by taking into account the experimental error inherent in the DEER modulation depth (0.003) and our CW EPR simulations (0.05). This information shows a relatively efficient loading of the Cu^{2+} into the CuQ_2 sites that is adequate for DEER distance measurements. DEER distance measurements themselves produce clean, narrow distance distributions that will aid in the unambiguous analysis of the data.

Molecular Dynamics Simulations. We utilized molecular dynamics (MD) simulations to understand the EPR results in an atomistic context. We constructed our initial PNA model for MD simulations in silico using PDB 2K4G as a starting template.[34] The geometry of each nucleobase and of the CuQ_2 groups was optimized using quantum mechanical calculations, and then force field parameters for each group were generated for use with the AMBER molecular simulation software.[95] The details are provided in the Methods section, and the force field parameters are included in the Supporting Information. Explicit bonds were formed between the Cu^{2+} atom and the coordinating oxygen and nitrogen atoms from both HQ groups.

With the PNA systems parameterized, we performed MD simulations of U-PNA for 100 ns. The distance between the two Cu^{2+} ions in the duplex was measured from frames of the simulation obtained every 10 ps. The distribution of these distances is shown as a red dashed line in Figure 4A, overlaid on the experimental DEER distance distribution. The MD distance distribution agrees well with both the most probable DEER distance and the total distribution width. This agreement indicates that the MD simulations accurately reproduced the overall structure and range of accessible conformations of the U-PNA duplex.

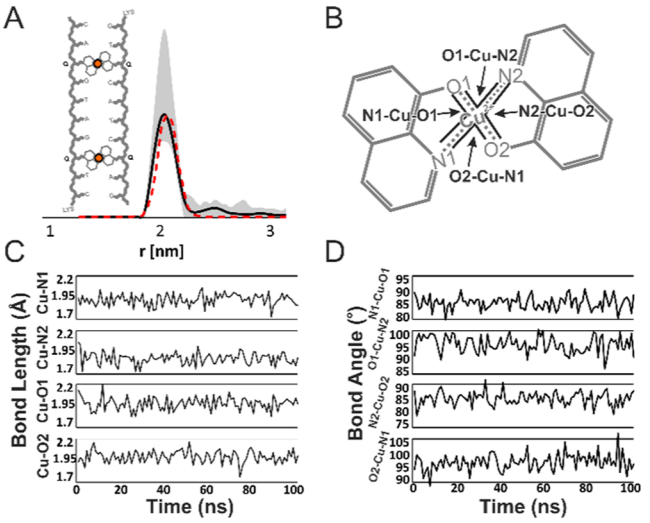

Figure 4. Results of the MD analysis of U-PNA. A) Distance distribution from MD (red dashed) compared to that measured by DEER (black). The experimental uncertainty is shown with gray shading. The MD Cu^{2+}−Cu^{2+} distribution is shown as a red dashed line. (B) Chemical structure of the CuQ_2 group. Coordinating atom names and Cu^{2+} bond angles are designated for reference. (C) Bond lengths between the Cu^{2+} and each coordinating oxygen and nitrogen sampled every 1 ns from the MD. (D) Cu^{2+} bond angles defined in (B) sampled every 1 ns.

Insight into the Orientational Selection in DEER from MD Results. We analyzed the Cu^{2+} coordination environment in the CuQ_2 complex, specifically the bond lengths and bond angles of the Cu^{2+} and its four coordinating atoms, obtained by MD simulations, and related it to the EPR results. First, we measured the coordination bond lengths from the central Cu^{2+} to each of the four coordinating atoms, as defined in Figure 4B. These bond lengths, sampled every 1 ns, are shown in Figure 4C. Each bond displayed an average (avg) length of approximately 1.9 Å with a standard deviation of 0.1 Å. These bond lengths are in good agreement with those found in typical Cu^{2+}−8-hydroxyquinoline complexes.[108,109] Next, we monitored the Cu^{2+} bond angles identified in Figure 4B. These angles are shown in Figure 4D. The O1−Cu−N2 and O2−Cu−N1 bond angles that involve coordinating atoms from different HQ ligands were ∼85 ± 2.5° (average ± s.d.). The N1−Cu−O1 and N2−Cu−O2 bond angles involving coordinating atoms from the same HQ ligand were ∼95 ± 3°. Each of these angles was found to fluctuate up to ±10° from their average value. The overall analysis of the CuQ_2 coordination shows variations in bond angles and lengths, a phenomenon that has been reported recently for another Cu^{2+} spin label.[94]

These variations in coordination environment, although subtle from a macromolecular viewpoint, have important implications on the *g*-tensor of the Cu^{2+}. We used ORCA to

https://dx.doi.org/10.1021/acs.jpcb.0c05509
J. Phys. Chem. B XXXX, XXX, XXX−XXX

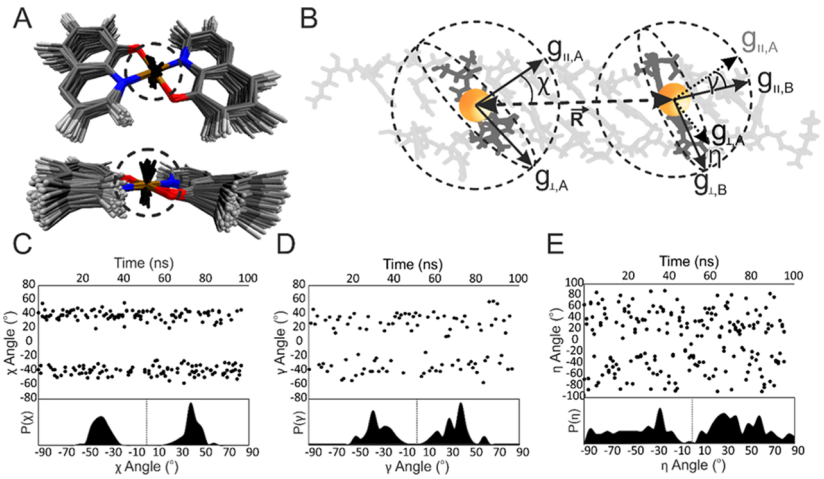

Figure 5. Orientational analysis of the CuQ_2 binding motif and its implications on EPR measurements. (A) Distribution of $g_{\|}$ directions (black lines) over the CuQ_2 structure as sampled every 1 ns of the MD run. *g*-Tensor calculations were performed with ORCA.[97,98] Individual structures were aligned to minimize the RMSD of the distances between the Cu^{2+} center and the four N and O coordinating atoms in each individual frame. (B) Definitions of each angle, χ, γ, and η, in the context of the U-PNA structure. These angles define the relative orientations of the CuQ_2 *g*-tensors. (C–E) Plots of the χ, γ, and η, respectively. The top charts show the angular values sampled every 1 ns. The bottom charts show the probability distribution of each angle.

calculate the *g*-tensor values and orientations for CuQ_2 from 100 frames evenly sampled throughout the MD simulation.[97,98] These calculations show that the value of $g_{\|}$ changes by 0.5%. To determine the extent of orientational fluctuation, we aligned each ORCA frame along the Cu^{2+} center and its four coordinating atoms by minimizing the RMSDs of the distances between equivalent atoms at each different frame. Based on this alignment of the Cu^{2+} local coordination environment, the orientation of $g_{\|}$ displayed a distribution of up to ~22.5° from its average orientation. This distribution in the orientations of *g*-tensors is shown as the black lines in Figure 5A. From this analysis, it is clear that the fluctuations in the Cu^{2+} coordination environment lead to a large distribution in orientation of the Cu^{2+} *g*-tensor. We note that in the distribution of $g_{\|}$ some individual axes are orientated "up" and "down" with respect to the plane defined by the Cu^{2+} and its coordinating atoms in the CuQ_2 complex. Previous analyses of $g_{\|}$ have elucidated a 180° symmetry of the $g_{\|}$ axis, as it is indistinguishable in the "upward" and "downward" orientations, and that the axis in either orientation produces the same DEER results.[110,115] Therefore, this finding is not unexpected.

Additionally, such changes in the orientations of $g_{\|}$ can profoundly affect the relative orientations of the *g*-tensors of each of the two Cu^{2+} spins. This relative orientation is described in terms of the three polar angles, χ, γ, and η, shown in Figure 5B. χ is the angle between the $g_{\|}$ axis of a Cu^{2+} center and the vector that connects the two Cu^{2+} centers, $\vec{R}$. γ is the angle between the $g_{\|}$ axes of the two Cu^{2+} centers. η is the angle between the $g_{\perp}$ axis of one Cu^{2+} and the projection of the second $g_{\perp}$ axis onto its perpendicular plane. Figure 5C–E shows these angles calculated from the 100 selected ORCA frames of the CuQ_2 complexes. Angle χ is bimodal with an average around ±40° and a standard deviation of 7°. The angle γ averages ±45° with a standard deviation of 20°, whereas η provides an even wider distribution of angles.

Previous work has shown that such a wide distribution of orientational angles is sufficient to ensure that the pulses used in DEER excite a wide range of molecular orientations, thereby "washing out" the effect of orientational selectivity,[94,114,125] which explains the DEER results shown in Figure 3. We can visualize and validate this point by aligning the $g_{\|}$ axes of one Cu^{2+} center and overlaying the U-PNA structure from each frame with the second Cu^{2+} displayed as spheres. Figure 6

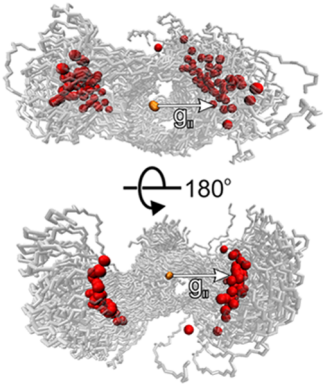

Figure 6. One hundred overlaid MD frames of U-PNA sampled every 1 ns along the MD trajectory, aligned along the $g_{\|}$ axis of one CuQ_2 site. The selected Cu^{2+} is shown as a sphere in the center, with the direction of the aligned $g_{\|}$ axis marked. Only the backbone atoms of the PNA duplex are displayed for simple viewing. The Cu^{2+} ions of the second CuQ_2 complex are also shown as red spheres. This figure emphasizes the many molecular orientations selected at a single $g_{\|}$ orientation.

shows the reference Cu^{2+} center as an orange sphere and the second Cu^{2+} center in the PNA duplex as red spheres. This figure reveals that the fluctuations of the Cu^{2+} coordination environment and consequential fluctuations in the direction of $g_{\|}$ drastically increase the molecular orientations that are sampled by the pump pulse in DEER at the single selected $g_{\|}$. With the finite bandwidth of pulses applied in DEER, the distribution in molecular orientations grows even larger. This analysis provides a clear conceptual understanding of the mechanism by which orientational selectivity is washed out in Cu^{2+} DEER at X-band frequencies.

Characterization of γ-Modified PNA by EPR and UV–Vis Spectroscopy. Next, we explored the utility of EPR as a

https://dx.doi.org/10.1021/acs.jpcb.0c05509
J. Phys. Chem. B XXXX, XXX, XXX–XXX

tool for the analysis of the structure of a γ-modified PNA duplex. Such data is important because the addition of substituent groups to the PNA backbone can be used to tailor the properties of the PNA. The PNA contained a hydroxymethyl modification on the γ-carbon of the peptide backbone in the base pairs adjacent to, or one base pair away from, the CuQ_2 sites (Figure 1).

As with the U-PNA, we performed CW and UV−vis measurements on the γ-PNA. The CW spectrum for γ-PNA (Figure 7A) is similar to that of the U-PNA. We determined

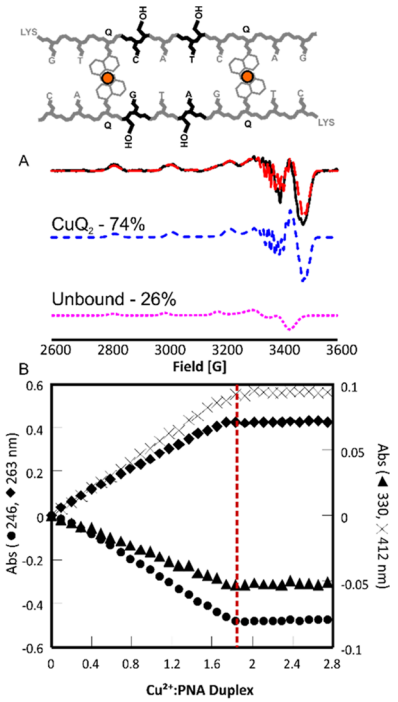

Figure 7. (A) CW EPR spectra of γ-PNA. The experimental CW spectrum is shown in black. The simulations of spectral components attributed to CuQ_2 sites and to nonspecifically bound Cu^{2+} are shown in blue dashed and pink dotted lines, respectively, below the experimental spectrum. The sum of the two components is shown as a red dashed line overlaid with the experimental data. (B) UV−vis titration curves for the γ-PNA duplex with Cu^{2+}.

the concentration of Cu^{2+} from the double-integrated intensity of the CW EPR spectrum, which again agreed with the expected concentration to within 5%. The spectrum of the γ-PNA was simulated using the EPR parameters determined for the U-PNA. From these simulations, we calculated the 74 ± 5% CuQ_2 loading. This loading efficiency is significantly lower than that measured for the U-PNA and may be due to alterations in the environment directly surrounding the Cu^{2+} binding site caused by the γ-modifications to bases directly adjacent to the CuQ_2 sites.[70]

The UV−vis titrations of γ-PNA in Figure 7B show a maximal Cu^{2+} binding at a 1.8:1 Cu^{2+}/PNA duplex, or 90 ± 5%, which differs from the CW simulation value of 74 ± 5%. This discrepancy may be due to differences in the duplex preparation, to differences in the concentration of the samples for UV−vis and EPR experiments, and/or to the presence of glycerol in the EPR samples. More specifically, for the UV−vis titration, the PNA duplex was first formed by annealing and then $CuCl_2$ was added into the solution containing the duplex, whereas for the EPR sample, the duplex was annealed in the presence of 2 equiv of Cu^{2+} (Figure S6). For the UV−vis experiments, the concentration of the samples is 5−10 μM; for the EPR samples, the Cu^{2+} concentration is 100−200 μM. Additionally, in EPR samples, glycerol must be used as a glassing agent and cryoprotectant because the EPR spectra are collected at 80 K, while glycerol was not added to the solution used in the UV−vis titrations.

Next, we performed DEER measurements on the γ-PNA (Figure 8A). As with the U-PNA, we see clear dipolar

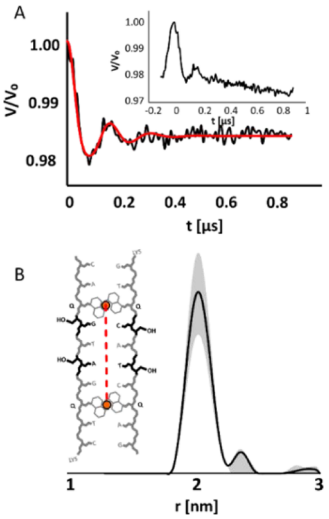

Figure 8. (A) Background-subtracted DEER signal with Tikhonov-regularized fit (red line) and raw time domain (inset) for γ-PNA. (B) Tikhonov-regularized DEER distance distribution, with a cartoon representation of γ-PNA (inset). The gray shading indicates the uncertainty of the distance measurement.

modulations in the DEER signal. The distance distribution between the two Cu^{2+} centers in the duplex is similar to that measured for U-PNA, with a most probable distance at 2 nm and a full width at half-height of 0.2 nm (Figure 8B). This observation suggests that the inclusion of only sparse γ-modifications in the PNA duplex does not cause significant changes in the range of PNA conformations. The analysis of the orientational angles for γ-PNA (Figure S7) led to angular distributions with similar averages and standard deviations as the U-PNA, making an experimental probe of orientational effects unnecessary. Therefore, the DEER was performed only at $g_\perp$.

The most notable difference between the DEER performed on γ-PNA and the U-PNA is in the modulation depth. γ-PNA shows a $\lambda = 0.016$ modulation depth compared to 0.059 for U-PNA. This result follows from the CW EPR findings that showed a reduced amount of the total Cu^{2+} bound in the γ-PNA. We analyzed the modulation depth on the γ-PNA by the method described above for U-PNA, under the same base assumptions. We used the component fractions determined by CW EPR, i.e. 74 ± 5% CuQ_2 binding and the values of λ = 0.016 and p_b of 0.051 determined from the EPR data.[124] We calculated $f_2 = 0.32 \pm 0.02$, $f_1 = 0.34 \pm 0.07$, and $f_N = 0.34 \pm 0.07$. Clearly, in the context of the EPR sample preparation conditions, the γ-modifications disrupt the loading efficiency of the CuQ_2 sites and lead to an ∼40% reduction in the population of doubly labeled PNAs. However, even with this decrease in loading efficiency, the EPR distance measurement

https://dx.doi.org/10.1021/acs.jpcb.0c05509
J. Phys. Chem. B XXXX, XXX, XXX−XXX

still provides a clear, narrow distance distribution that is well suited for conformational determination.

MD Simulations and DEER Distance Measurements Provide Atomistic Insight into the PNA Structure. Following the DEER measurements, we generated an initial structure for the duplex and force field parameters for the γ-modified base pairs and performed MD simulations on γ-PNA for 100 ns (Figure 9). The Cu^{2+}−Cu^{2+} distance distribution

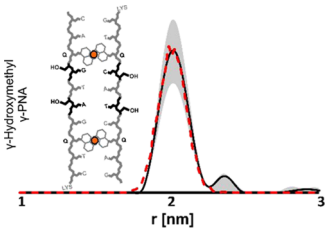

Figure 9. MD simulation results for γ-PNA. The distance distributions showing the Tikhonov-regularized DEER distribution in black with uncertainty analysis (gray shading). The MD Cu^{2+}−Cu^{2+} distribution is shown as a red dashed line.

obtained for the MD simulations (red dashed line in Figure 9) agrees well with the distance distribution obtained from EPR. Again, this agreement applies to both the most probable distance and the width of the distribution. Based on these results, we believe that EPR distance methods in conjunction with MD simulations are applicable to PNA systems containing γ-modifications.

Next, we analyzed the trajectories of both the U-PNA and γ-PNA to gain atomistic-level insight into the structures. To this end, we extracted all of the trajectory frames from the MD simulations from U-PNA and γ-PNA that displayed Cu^{2+}−Cu^{2+} distances within the ranges of 1.85−1.95, 1.95−2.05, and 2.05−2.15 nm (Figure 10). These distance ranges correspond to the shortest, most probable, and longest accessible CuQ_2−CuQ_2 distances from the DEER distributions, respectively. Each distance range contained 1000−4000 individual frames.

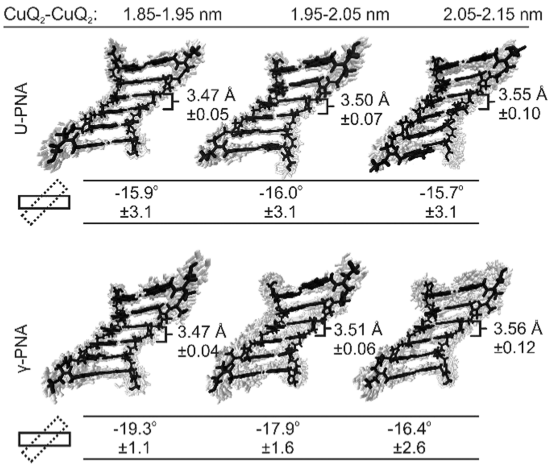

Figure 10. Average structure of U-PNA (top) and γ-PNA (bottom) taken from all frames of the MD simulation that had a CuQ_2−CuQ_2 distance in the range indicated above each structure. The average structure (black) is overlaid atop the individual frames comprising it (light gray). Noted alongside the structures are the average rises of the PNA base pairs (avg ± s.d.). Underneath the structures are the average twist angles of the PNA duplex (avg ± s.d.).[126]

Each set of structures was then averaged to produce a representative structure for each distance range. We analyzed and compared various helical parameters of these average structures from the core base pairs found between the CuQ_2 residues using 3DNA.[127] The average rise, or vertical displacement between base pairs, is noted next to each average structure in Figure 10. The average twist of each base pair in degrees is noted underneath each structure.

This analysis reveals that there is little backbone fluctuation across all sampled PNA conformations, which is not surprising given the very narrow distance distribution revealed by the DEER signals. The average rise per base pair of both the U-PNA and the γ-PNA, in their most probable conformations, i.e., the one in which the CuQ_2−CuQ_2 distance is between 1.95 and 2.05 nm, is ∼3.5 Å. The average rise per base pair calculated by the MD simulations agrees well with the value of 3.2 Å obtained by X-ray crystallography and NMR spectroscopy.[18] These results show that the overall double-helical shape of the PNA is not affected by the addition of CuQ_2 groups. This conclusion is further supported by circular dichroism data, which shows a signal typical of double-helical PNA (Figure S6).

Analysis of the twist angles revealed subtle differences between the conformations of the U-PNA and the γ-PNA. For the U-PNA, the average twist angle is the same in each distance range (within the standard deviation). For the γ-PNA, the average twist angle decreases and the corresponding standard deviation increases as the Cu^{2+}−Cu^{2+} distance increases. Also notable is that the standard deviations of the twist angles of the γ-PNA are lower than those of the U-PNA. This result indicates a narrower range of accessible conformations for the γ-PNA than for the U-PNA. Furthermore, the RMSD and root-mean-square fluctuation (RMSF) of the U-PNA compared to those of the γ-PNA are similar (Figures S8 and S9, respectively).

These results suggest that the inclusion of sparse γ-modifications in the PNA backbone has subtle effects on the conformations of the PNA duplex, specifically with regard to the twist angles. The conformation of U-PNA varies mainly in the rise per base pair while the twist angles remain constant. The γ-PNA shows variations in both the rise of the base pairs and the twist of the helix.

CONCLUSIONS

We have measured for the first time distances between two Cu^{2+}-based spin labels within a PNA duplex by EPR. We found that the CuQ_2 spin labeling motif is efficient and effective for the measurement of distances within standard aeg-based PNA duplexes as well as within PNA duplexes with γ-modifications. We have developed MD force field parameters that can be used to accurately simulate the PNA canonical nucleobases, a backbone with modifications, and CuQ_2 motif in the PNA. Such methods for the measurement of distances by EPR interpreted with the additional context of MD simulations have enabled us to gain an atomistic understanding of the PNA structure. These advancements represent an important avenue for the elucidation of PNA conformational changes. Additionally, the atomistic information provided by MD coupled with the EPR results clearly demonstrates that small fluctuations in the Cu^{2+} coordination environment induced from the elasticity of Cu^{2+} binding lead to large distributions in the *g*-tensor orientation, sufficient enough to "wash out" any orientational selectivity at X-band. Therefore, the Cu^{2+}−Cu^{2+} distance can

https://dx.doi.org/10.1021/acs.jpcb.0c05509
J. Phys. Chem. B XXXX, XXX, XXX−XXX

be measured through a single experiment performed at $g_\perp$ at X-band frequencies despite the rigidity of the spin label. Overall, this development of EPR and MD methods expands the toolset available for the analysis and assessment of PNA's structure and conformations.

■ ASSOCIATED CONTENT

Supporting Information

The Supporting Information is available free of charge at https://pubs.acs.org/doi/10.1021/acs.jpcb.0c05509.

Chemical structures of force field parameterized PNA subunits, CW EPR spectra at multiple microwave powers to test for signal saturation, full chemical structures of the PNA duplexes, control CW EPR spectrum of $CuCl_2$ in phosphate buffer, UV−vis spectra of PNA-Cu^{2+} titrations for U-PNA and γ-PNA, CD spectra and melting curves of U-PNA and γ-PNA, probability distributions of relative orientational angles for γ-PNA, RMSD, and RMSF plots for U-PNA and γ-PNA, and residue topologies and force field parameters for all PNA subunits (PDF)

■ AUTHOR INFORMATION

Corresponding Authors

Junmei Wang − *Department of Pharmaceutical Sciences, University of Pittsburgh, Pittsburgh, Pennsylvania 15206, United States;* orcid.org/0000-0002-9607-8229; Phone: 412 383 3268; Email: juw79@pitt.edu

Catalina Achim − *Department of Chemistry, Carnegie Mellon University, Pittsburgh, Pennsylvania 15213, United States;* orcid.org/0000-0001-5420-4656; Email: achim@cmu.edu

Sunil Saxena − *Department of Chemistry, University of Pittsburgh, Pittsburgh, Pennsylvania 15260, United States;* orcid.org/0000-0001-9098-6114; Phone: 412 624 8680; Email: sksaxena@pitt.edu

Authors

Austin Gamble Jarvi − *Department of Chemistry, University of Pittsburgh, Pittsburgh, Pennsylvania 15260, United States*

Artur Sargun − *Department of Chemistry, Carnegie Mellon University, Pittsburgh, Pennsylvania 15213, United States*

Xiaowei Bogetti − *Department of Chemistry, University of Pittsburgh, Pittsburgh, Pennsylvania 15260, United States*

Complete contact information is available at: https://pubs.acs.org/10.1021/acs.jpcb.0c05509

Author Contributions

The manuscript was written through the contributions of all authors. All authors have given approval to the final version of the manuscript.

Notes

The authors declare no competing financial interest.

■ ACKNOWLEDGMENTS

S.S. acknowledges NSF MCB-1613007. The EPR spectrometer was supported by NSF MRI-1725678 to S.S. C.A. acknowledges NSF support (CHE-1310441). J.W. acknowledges NIH support (R01-GM079383 and P30-DA035778). The Center for Molecular Analysis at Carnegie Mellon University was supported in part by the NSF (CHE-9808188 and DBI-9729351). All MD simulations were performed at the University of Pittsburgh's Center for Research Computing. The authors thank Dr. Marcela Madrid (Pittsburgh Supercomputing Center) for her early discussions relating to the molecular dynamics parameterization.

■ ABBREVIATIONS

EPR, electron paramagnetic resonance; MD, molecular dynamics; CW, continuous wave; PNA, peptide nucleic acid; HQ, 8-hydroxyquinoline; aeg, aminoethylglycine

■ REFERENCES

(1) Seeman, N. C. Nucleic Acid Nanostructures and Topology. *Angew. Chem., Int. Ed.* **1998**, *37*, 3220−3238.

(2) Goodman, R. P.; Heilemann, M.; Doose, S.; Erben, C. M.; Kapanidis, A. N.; Turberfield, A. J. Reconfigurable, Braced, Three-Dimensional DNA Nanostructures. *Nat. Nanotechnol.* **2008**, *3*, 93−96.

(3) Wilner, O. I.; Willner, I. Functionalized DNA Nanostructures. *Chem. Rev.* **2012**, *112*, 2528−2556.

(4) Seeman, N. C. From Genes to Machines: DNA Nanomechanical Devices. *Trends Biochem. Sci.* **2005**, *30*, 119−125.

(5) Bath, J.; Turberfield, A. J. DNA Nanomachines. *Nat. Nanotechnol.* **2007**, *2*, 275−284.

(6) Ramezani, H.; Dietz, H. Building Machines with DNA Molecules. *Nat. Rev. Genet.* **2020**, *21*, 5−26.

(7) Saidur, M. R.; Aziz, A. R. A.; Basirun, W. J. Recent Advances in DNA-Based Electrochemical Biosensors for Heavy Metal Ion Detection: A Review. *Biosens. Bioelectron.* **2017**, *90*, 125−139.

(8) Chao, J.; Zhu, D.; Zhang, Y.; Wang, L.; Fan, C. DNA Nanotechnology-Enabled Biosensors. *Biosens. Bioelectron.* **2016**, *76*, 68−79.

(9) Huang, R.; He, N.; Li, Z. Recent Progresses in DNA Nanostructure-Based Biosensors for Detection of Tumor Markers. *Biosens. Bioelectron.* **2018**, *109*, 27−34.

(10) de Vries, J. W.; Zhang, F.; Herrmann, A. Drug Delivery Systems Based on Nucleic Acid Nanostructures. *J. Controlled Release* **2013**, *172*, 467−483.

(11) Linko, V.; Ora, A.; Kostiainen, M. A. DNA Nanostructures as Smart Drug-Delivery Vehicles and Molecular Devices. *Trends Biotechnol.* **2015**, *33*, 586−594.

(12) Hu, Q.; Li, H.; Wang, L.; Gu, H.; Fan, C. DNA Nanotechnology-Enabled Drug Delivery Systems. *Chem. Rev.* **2019**, *119*, 6459−6506.

(13) Lächelt, U.; Wagner, E. Nucleic Acid Therapeutics Using Polyplexes: A Journey of 50 Years (and Beyond). *Chem. Rev.* **2015**, *115*, 11043−11078.

(14) Sridharan, K.; Gogtay, N. J. Therapeutic Nucleic Acids: Current Clinical Status. *Br. J. Clin. Pharmacol.* **2016**, *82*, 659−672.

(15) Takemoto, K.; Inaki, Y. *Synthetic Nucleic Acid Analogs Preparation and Interaction*; Springer: Berlin, Heidelberg, 1981; pp 1−51.

(16) Benner, S. A.; Karalkar, N. B.; Hoshika, S.; Laos, R.; Shaw, R. W.; Matsuura, M.; Fajardo, D.; Moussatche, P. Alternative Watson−Crick Synthetic Genetic Systems. *Cold Spring Harbor Perspect. Biol.* **2016**, *8*, No. a023770.

(17) Egholm, M.; Buchardt, O.; Nielsen, P. E.; Berg, R. H. Peptide Nucleic Acids (PNA). Oligonucleotide Analogs with an Achiral Peptide Backbone. *J. Am. Chem. Soc.* **1992**, *114*, 1895−1897.

(18) Nielsen, P. E.; Egholm, M. An Introduction to Peptide Nucleic Acid. *Curr. Issues Mol. Biol.* **1999**, *1*, 89−104.

(19) Egholm, M.; Buchardt, O.; Christensen, L.; Behrens, C.; Freier, S. M.; Driver, D. A.; Berg, R. H.; Kim, S. K.; Norden, B.; Nielsen, P. E. PNA Hybridizes to Complementary Oligonucleotides Obeying the Watson−Crick Hydrogen-Bonding Rules. *Nature* **1993**, *365*, 566−568.

(20) Wittung, P.; Nielsen, P. E.; Buchardt, O.; Egholm, M.; Norde′n, B. DNA-Like Double Helix Formed by Peptide Nucleic Acid. *Nature* **1994**, *368*, 561−563.

(21) Jensen, K. K.; Ørum, H.; Nielsen, P. E.; Nordén, B. Kinetics for Hybridization of Peptide Nucleic Acids (PNA) with DNA and Rna

Studied with the Biacore Technique. *Biochemistry* **1997**, *36*, 5072−5077.
(22) Demidov, V. V.; Potaman, V. N.; Frank-Kamenetskil, M. D.; Egholm, M.; Buchard, O.; Sönnichsen, S. H.; Nlelsen, P. E. Stability of Peptide Nucleic Acids in Human Serum and Cellular Extracts. *Biochem. Pharmacol.* **1994**, *48*, 1310−1313.
(23) De Mesmaeker, A.; Altmann, K.-H.; Waldner, A.; Wendeborn, S. Backbone Modifications in Oligonucleotides and Peptide Nucleic Acid Systems. *Curr. Opin. Struct. Biol.* **1995**, *5*, 343−355.
(24) Nielsen, P. E. Applications of Peptide Nucleic Acids. *Curr. Opin. Biotechnol.* **1999**, *10*, 71−75.
(25) Saarbach, J.; Sabale, P. M.; Winssinger, N. Peptide Nucleic Acid (PNA) and Its Applications in Chemical Biology, Diagnostics, and Therapeutics. *Curr. Opin. Chem. Biol.* **2019**, *52*, 112−124.
(26) Gourishankar, A.; Shukla, S.; Pasricha, R.; Sastry, M.; Ganesh, K. N. DNA and PNA as Templates for Building Nanoassemblies Via Electrostatic Complexation with Gold Nanoparticles. *Curr. Appl. Phys.* **2005**, *5*, 102−107.
(27) Beall, E.; Ulku, S.; Liu, C.; Wierzbinski, E.; Zhang, Y.; Bae, Y.; Zhang, P.; Achim, C.; Beratan, D. N.; Waldeck, D. H. Effects of the Backbone and Chemical Linker on the Molecular Conductance of Nucleic Acid Duplexes. *J. Am. Chem. Soc.* **2017**, *139*, 6726−6735.
(28) Feldkamp, U.; Niemeyer, C. M. Rational Design of DNA Nanoarchitectures. *Angew. Chem., Int. Ed.* **2006**, *45*, 1856−1876.
(29) Paul, A.; Bezer, S.; Venkatramani, R.; Kocsis, L.; Wierzbinski, E.; Balaeff, A.; Keinan, S.; Beratan, D. N.; Achim, C.; Waldeck, D. H. Role of Nucleobase Energetics and Nucleobase Interactions in Single-Stranded Peptide Nucleic Acid Charge Transfer. *J. Am. Chem. Soc.* **2009**, *131*, 6498−6507.
(30) Paul, A.; Watson, R. M.; Wierzbinski, E.; Davis, K. L.; Sha, A.; Achim, C.; Waldeck, D. H. Distance Dependence of the Charge Transfer Rate for Peptide Nucleic Acid Monolayers. *J. Phys. Chem. B* **2010**, *114*, 14140−14148.
(31) Wierzbinski, E.; de Leon, A.; Yin, X.; Balaeff, A.; Davis, K. L.; Reppireddy, S.; Venkatramani, R.; Keinan, S.; Ly, D. H.; Madrid, M.; et al. Effect of Backbone Flexibility on Charge Transfer Rates in Peptide Nucleic Acid Duplexes. *J. Am. Chem. Soc.* **2012**, *134*, 9335−9342.
(32) Eriksson, M.; Nielsen, P. E. Solution Structure of a Peptide Nucleic Acid−DNA Duplex. *Nat. Struct. Biol.* **1996**, *3*, 410−413.
(33) Yeh, J. I.; Pohl, E.; Truan, D.; He, W.; Sheldrick, G. M.; Du, S.; Achim, C. The Crystal Structure of Non-Modified and Bipyridine-Modified PNA Duplexes. *Chem. − Eur. J.* **2010**, *16*, 11867−11875.
(34) He, W.; Hatcher, E.; Balaeff, A.; Beratan, D. N.; Gil, R. R.; Madrid, M.; Achim, C. Solution Structure of a Peptide Nucleic Acid Duplex from NMR Data: Features and Limitations. *J. Am. Chem. Soc.* **2008**, *130*, 13264−13273.
(35) Roessler, M. M.; Salvadori, E. Principles and Applications of EPR Spectroscopy in the Chemical Sciences. *Chem. Soc. Rev.* **2018**, *47*, 2534−2553.
(36) Jeschke, G. The Contribution of Modern EPR to Structural Biology. *Emerging Top. Life Sci.* **2018**, *2*, 9−18.
(37) Saxena, S.; Freed, J. H. Double Quantum Two Dimensional Fourier Transform Electron Spin Resonance: Distance Measurements. *Chem. Phys. Lett.* **1996**, *251*, 102.
(38) Borbat, P. P.; Freed, J. H. Multiple-Quantum ESR and Distance Measurements. *Chem. Phys. Lett.* **1999**, *313*, 145−154.
(39) Milov, A.; Maryasov, A.; Tsvetkov, Y. D. Pulsed Electron Double Resonance (Peldor) and Its Applications in Free-Radicals Research. *Appl. Magn. Reson.* **1998**, *15*, 107−143.
(40) Pannier, M.; Veit, S.; Godt, A.; Jeschke, G.; Spiees, H. W. Dead-Time Free Measurement of Dipole-Dipole Interactions between Electron Spins. *J. Magn. Reson.* **2000**, *142*, 331−340.
(41) Kulik, L. V.; Grishin, Y. A.; Dzuba, S. A.; Grigoryev, I. A.; Klyatskaya, S. V.; Vasilevsky, S. F.; Tsvetkov, Y. D. Electron Dipole−Dipole Eseem in Field-Step Eldor of Nitroxide Biradicals. *J. Magn. Reson.* **2002**, *157*, 61−68.
(42) Milikisyants, S.; Scarpelli, F.; Finiguerra, M. G.; Ubbink, M.; Huber, M. A Pulsed EPR Method to Determine Distances between Paramagnetic Centers with Strong Spectral Anisotropy and Radicals: The Dead-Time Free Ridme Sequence. *J. Magn. Reson.* **2009**, *201*, 48−56.
(43) Jeschke, G.; Pannier, M.; Godt, A.; Spiess, H. W. Dipolar Spectroscopy and Spin Alignment in Electron Paramagnetic Resonance. *Chem. Phys. Lett.* **2000**, *331*, 243−252.
(44) Hubbell, W. L.; Altenbach, C. Investigation of Structure and Dynamics in Membrane Proteins Using Site-Directed Spin Labeling. *Cur. Opin. Struct. Biol.* **1994**, *4*, 566−573.
(45) Fanucci, G. E.; Cafiso, D. S. Recent Advances and Applications of Site-Directed Spin Labeling. *Curr. Opin. Struct. Biol.* **2006**, *16*, 644−653.
(46) Hubbell, W. L.; López, C. J.; Altenbach, C.; Yang, Z. Technological Advances in Site-Directed Spin Labeling of Proteins. *Curr. Opin. Struct. Biol.* **2013**, *23*, 725−733.
(47) Becker, J. S.; Saxena, S. Double Quantum Coherence Electron Spin Resonance on Coupled Cu(II)−Cu(II) Electron Spins. *Chem. Phys. Lett.* **2005**, *414*, 248−252.
(48) Yang, Z.; Becker, J.; Saxena, S. On Cu(II)−Cu(II) Distance Measurements Using Pulsed Electron Electron Double Resonance. *J. Magn. Reson.* **2007**, *188*, 337−343.
(49) Yang, Z.; Ji, M.; Cunningham, T. F.; Saxena, S. Cu^{2+} as an ESR Probe of Protein Structure and Function. *Methods in Enzymology*; Elsevier, 2015; Vol. *563*, pp 459−481.
(50) Cunningham, T. F.; Shannon, M. D.; Putterman, M. R.; Arachchige, R. J.; Sengupta, I.; Gao, M.; Jaroniec, C. P.; Saxena, S. Cysteine-Specific Cu2+ Chelating Tags Used as Paramagnetic Probes in Double Electron Electron Resonance. *J. Phys. Chem. B* **2015**, *119*, 2839−2843.
(51) Cunningham, T. F.; Putterman, M. R.; Desai, A.; Horne, W. S.; Saxena, S. The Double-Histidine Cu2+-Binding Motif: A Highly Rigid, Site-Specific Spin Probe for Electron Spin Resonance Distance Measurements. *Angew. Chem., Int. Ed.* **2015**, *54*, 6330−6334.
(52) Lawless, M. J.; Ghosh, S.; Cunningham, T. F.; Shimshi, A.; Saxena, S. On the Use of the Cu2+−Iminodiacetic Acid Complex for Double Histidine Based Distance Measurements by Pulsed ESR. *Phys. Chem. Chem. Phys.* **2017**, *19*, 20959−20967.
(53) Ghosh, S.; Lawless, M. J.; Rule, G. S.; Saxena, S. The Cu2+-Nitrilotriacetic Acid Complex Improves Loading of A-Helical Double Histidine Site for Precise Distance Measurements by Pulsed ESR. *J. Magn. Reson.* **2018**, *286*, 163−171.
(54) Merz, G. E.; Borbat, P. P.; Muok, A. R.; Srivastava, M.; Bunck, D. N.; Freed, J. H.; Crane, B. R. Site-Specific Incorporation of a Cu2+ Spin Label into Proteins for Measuring Distances by Pulsed Dipolar Electron Spin Resonance Spectroscopy. *J. Phys. Chem. B* **2018**, *122*, 9443−9451.
(55) Sarver, J.; Silva, K. I.; Saxena, S. Measuring Cu2+-Nitroxide Distances Using Double Electron−Electron Resonance and Saturation Recovery. *Appl. Magn. Reson.* **2013**, *44*, 583−594.
(56) Raitsimring, A. M.; Gunanathan, C.; Potapov, A.; Efremenko, I.; Martin, J. M. L.; Milstein, D.; Goldfarb, D. Gd3+ Complexes as Potential Spin Labels for High Field Pulsed EPR Distance Measurements. *J. Am. Chem. Soc.* **2007**, *129*, 14138−14139.
(57) Yulikov, M.; Lueders, P.; Farooq Warsi, M.; Chechik, V.; Jeschke, G. Distance Measurements in Au Nanoparticles Functionalized with Nitroxide Radicals and Gd3+−Dtpa Chelate Complexes. *Phys. Chem. Chem. Phys.* **2012**, *14*, 10732−10746.
(58) Goldfarb, D. Gd3+ Spin Labeling for Distance Measurements by Pulse EPR Spectroscopy. *Phys. Chem. Chem. Phys.* **2014**, *16*, 9685−9699.
(59) Barthelmes, D.; Gränz, M.; Barthelmes, K.; Allen, K. N.; Imperiali, B.; Prisner, T.; Schwalbe, H. Encoded Loop-Lanthanide-Binding Tags for Long-Range Distance Measurements in Proteins by NMR and EPR Spectroscopy. *J. Biomol. NMR* **2015**, *63*, 275−282.
(60) Abdelkader, E. H.; Lee, M. D.; Feintuch, A.; Cohen, M. R.; Swarbrick, J. D.; Otting, G.; Graham, B.; Goldfarb, D. A New Gd3+ Spin Label for Gd3+−Gd3+ Distance Measurements in Proteins Produces Narrow Distance Distributions. *J. Phys. Chem. Lett.* **2015**, *6*, 5016−5021.

https://dx.doi.org/10.1021/acs.jpcb.0c05509
J. Phys. Chem. B XXXX, XXX, XXX−XXX

(61) Mascali, F. C.; Ching, H. Y. V.; Rasia, R. M.; Un, S.; Tabares, L. C. Using Genetically Encodable Self-Assembling GdIII Spin Labels to Make in-Cell Nanometric Distance Measurements. *Angew. Chem., Int. Ed.* **2016**, *55*, 11041−11043.
(62) Prokopiou, G.; Lee, M. D.; Collauto, A.; Abdelkader, E. H.; Bahrenberg, T.; Feintuch, A.; Ramirez-Cohen, M.; Clayton, J.; Swarbrick, J. D.; Graham, B.; et al. Small Gd(III) Tags for Gd(III)−Gd(III) Distance Measurements in Proteins by EPR Spectroscopy. *Inorg. Chem.* **2018**, *57*, 5048−5059.
(63) Banerjee, D.; Yagi, H.; Huber, T.; Otting, G.; Goldfarb, D. Nanometer-Range Distance Measurement in a Protein Using Mn2+ Tags. *J. Phys. Chem. Lett.* **2012**, *3*, 157−160.
(64) Martorana, A.; Yang, Y.; Zhao, Y.; Li, Q.-F.; Su, X.-C.; Goldfarb, D. Mn(Ii) Tags for Deer Distance Measurements in Proteins Via C−S Attachment. *Dalton Trans.* **2015**, *44*, 20812−20816.
(65) Akhmetzyanov, D.; Plackmeyer, J.; Endeward, B.; Denysenkov, V.; Prisner, T. F. Pulsed Electron−Electron Double Resonance Spectroscopy between a High-Spin Mn2+ Ion and a Nitroxide Spin Label. *Phys. Chem. Chem. Phys.* **2015**, *17*, 6760−6766.
(66) Keller, K.; Zalibera, M.; Qi, M.; Koch, V.; Wegner, J.; Hintz, H.; Godt, A.; Jeschke, G.; Savitsky, A.; Yulikov, M. EPR Characterization of Mn(Ii) Complexes for Distance Determination with Pulsed Dipolar Spectroscopy. *Phys. Chem. Chem. Phys.* **2016**, *18*, 25120−25135.
(67) Abdullin, D.; Schiemann, O. Pulsed Dipolar EPR Spectroscopy and Metal Ions: Methodology and Biological Applications. *ChemPlusChem* **2020**, *85*, 353−372.
(68) Shelke, S. A.; Sigurdsson, S. T. Site-Directed Spin Labeling for EPR Studies of Nucleic Acids. In *Modified Nucleic Acids*; Nakatani, K.; Tor, Y., Eds.; Springer International Publishing: Cham, 2016; pp 159−187.
(69) Lawless, M. J.; Sarver, J. L.; Saxena, S. Nucleotide-Independent Copper (II)-Based Distance Measurements in DNA by Pulsed ESR Spectroscopy. *Angew. Chem., Int. Ed.* **2017**, *56*, 2115−2117.
(70) Ghosh, S.; Lawless, M. J.; Brubaker, H. J.; Singewald, K.; Kurpiewski, M. R.; Jen-Jacobson, L.; Saxena, S. Cu2+-Based Distance Measurements by Pulsed EPR Provide Distance Constraints for DNA Backbone Conformations in Solution. *Nucleic Acids Res.* **2020**, No. e49.
(71) Li, X.; Cheng, Y.; Zhang, L.; Zhang, L. Synthesis of Spin Labeled Conjugate of Peptide and Peptide Nucleic Acid. *Synth. Commun.* **1999**, *29*, 1519−1525.
(72) Cerasi, A.; Millo, E.; Ottaviani, M. F.; Damonte, G.; Cangiotti, M.; Benatti, U.; Chiarantini, L. New Synthesis of a Spin-Labeled Peptide Nucleic Acid and Its Interactions with Nucleic Acids. *Tetrahedron Lett.* **2003**, *44*, 8701−8704.
(73) Li, X.; Huang, C.; Wang, Y.; Chen, Y.; Zhang, L.; Lu, J.; Zhang, L. Studies on Spin-Labelled Peptide Nucleic Acid. *Curr. Sci.* **1998**, *74*, 624−626.
(74) Marinelli, F.; Faraldo-Gómez, J. D. Ensemble-Biased Metadynamics: A Molecular Simulation Method to Sample Experimental Distributions. *Biophys. J.* **2015**, *108*, 2779−2782.
(75) Marinelli, F.; Fiorin, G. Structural Characterization of Biomolecules through Atomistic Simulations Guided by Deer Measurements. *Structure* **2019**, *27*, No. 359.e12.
(76) Verhalen, B.; Dastvan, R.; Thangapandian, S.; Peskova, Y.; Koteiche, H. A.; Nakamoto, R. K.; Tajkhorshid, E.; McHaourab, H. S. Energy Transduction and Alternating Access of the Mammalian Abc Transporter P-Glycoprotein. *Nature* **2017**, *543*, 738.
(77) Shen, R.; Han, W.; Fiorin, G.; Islam, S. M.; Schulten, K.; Roux, B. Structural Refinement of Proteins by Restrained Molecular Dynamics Simulations with Non-Interacting Molecular Fragments. *PLoS Comput. Biol.* **2015**, *11*, No. e1004368.
(78) Ding, F.; Layten, M.; Simmerling, C. Solution Structure of Hiv-1 Protease Flaps Probed by Comparison of Molecular Dynamics Simulation Ensembles and EPR Experiments. *J. Am. Chem. Soc.* **2008**, *130*, 7184−7185.
(79) Sarver, J. L.; Townsend, J. E.; Rajapakse, G.; Jen-Jacobson, L.; Saxena, S. Simulating the Dynamics and Orientations of Spin-Labeled Side Chains in a Protein−DNA Complex. *J. Phys. Chem. B* **2012**, *116*, 4024−4033.
(80) Sale, K.; Song, L.; Liu, Y.-S.; Perozo, E.; Fajer, P. Explicit Treatment of Spin Labels in Modeling of Distance Constraints from Dipolar EPR and Deer. *J. Am. Chem. Soc.* **2005**, *127*, 9334−9335.
(81) Sen, S.; Nilsson, L. Molecular Dynamics of Duplex Systems Involving PNA: Structural and Dynamical Consequences of the Nucleic Acid Backbone. *J. Am. Chem. Soc.* **1998**, *120*, 619−631.
(82) Weroński, P.; Jiang, Y.; Rasmussen, S. Molecular Dynamics Study of Small PNA Molecules in Lipid-Water System. *Biophys. J.* **2007**, *92*, 3081−3091.
(83) Autiero, I.; Saviano, M.; Langella, E. Molecular Dynamics Simulations of PNA−PNA and PNA−DNA Duplexes by the Use of New Parameters Implemented in the Gromacs Package: A Conformational and Dynamics Study. *Phys. Chem. Chem. Phys.* **2014**, *16*, 1868−1874.
(84) Soliva, R.; Sherer, E.; Luque, F. J.; Laughton, C. A.; Orozco, M. Molecular Dynamics Simulations of PNA·DNA and PNA·Rna Duplexes in Aqueous Solution. *J. Am. Chem. Soc.* **2000**, *122*, 5997−6008.
(85) Jasiński, M.; Feig, M.; Trylska, J. Improved Force Fields for Peptide Nucleic Acids with Optimized Backbone Torsion Parameters. *J. Chem. Theory Comput.* **2018**, *14*, 3603−3620.
(86) Stoll, S.; Schweiger, A. Easyspin, a Comprehensive Software Package for Spectral Simulation and Analysis in EPR. *J. Magn. Reson.* **2006**, *178*, 42−55.
(87) Chiang, Y.-W.; Borbat, P. P.; Freed, J. H. The Determination of Pair Distance Distributions by Pulsed ESR Using Tikhonov Regularization. *J. Magn. Reson.* **2005**, *172*, 279−295.
(88) Jeschke, G.; Chechik, V.; Ionita, P.; Godt, A.; Zimmermann, H.; Banham, J.; Timmel, C. R.; Hilger, D.; Jung, H. Deeranalysis2006—a Comprehensive Software Package for Analyzing Pulsed Eldor Data. *Appl. Magn. Reson.* **2006**, *30*, 473−498.
(89) Frisch, M. J.; Trucks, G. W.; Schlegel, H. B.; Scuseria, G. E.; Robb, M. A.; Cheeseman, J. R.; Scalmani, G.; Barone, V.; Petersson, G. A.; Nakatsuji, H. et al. *Gaussian 16*, revision C.01; Gaussian, Inc.: Wallingford, CT, 2016.
(90) Bayly, C. I.; Cieplak, P.; Cornell, W. D.; Kollman, P. A. A Well-Behaved Electrostatic Potential Based Method Using Charge Restraints for Deriving Atomic Charges- the Resp Model. *J. Phys. Chem. A* **1993**, *97*, 10269−10280.
(91) Wang, J.; Wang, W.; Kollman, P. A.; Case, D. A. Automatic Atom Type and Bond Type Perception in Molecular Mechanical Calculations. *J. Mol. Graphics Modell.* **2006**, *25*, 247−260.
(92) Case, D. A.; Ben-Shalom, I. Y.; Brozell, S. R.; Cerutti, D. S.; Cheatham, T. E., III; Cruzeiro, V. W. D.; Darden, T. A.; Duke, R. E.; Ghoreishi, D.; Gilson, M. K. et al. *Amber 2018*; University of California: San Francisco, 2018.
(93) Wang, J.; Wolf, R. M.; Caldwell, J. W.; Kollman, P. A.; Case, D. A. Development and Testing of a General Amber Force Field. *J. Comput. Chem.* **2004**, *25*, 1157−1174.
(94) Bogetti, X.; Ghosh, S.; Gamble Jarvi, A.; Wang, J.; Saxena, S. Molecular Dynamics Simulations Based on Newly Developed Force Field Parameters for Cu2+ Spin Labels Provide Insights into Double-Histidine-Based Double Electron−Electron Resonance. *J. Phys. Chem. B* **2020**, *124*, 2788−2797.
(95) Case, D.; Betz, R.; Botello-Smith, W.; Cerutti, D.; Darden, T. *Amber 2016*; University of California: San Fransico, 2016.
(96) Jorgensen, W. L.; Chandrasekhar, J.; Madura, J. D.; Impey, R. W.; Klein, M. L. Comparison of Simple Potential Functions for Simulating Liquid Water. *J. Chem. Phys.* **1983**, *79*, 926−935.
(97) Neese, F. The Orca Program System. *WIREs Comput. Mol. Sci.* **2012**, *2*, 73−78.
(98) Neese, F. Software Update: The Orca Program System, Version 4.0. *WIREs Comput. Mol. Sci.* **2018**, *8*, No. e1327.
(99) Humphrey, W.; Dalke, A.; Schulten, K. Vmd: Visual Molecular Dynamics. *J. Mol. Graphics* **1996**, *14*, 33−38.
(100) Christensen, L.; Fitzpatrick, R.; Gildea, B.; Petersen, K. H.; Hansen, H. F.; Koch, T.; Egholm, M.; Buchardt, O.; Nielsen, P. E.;

https://dx.doi.org/10.1021/acs.jpcb.0c05509
J. Phys. Chem. B XXXX, XXX, XXX−XXX

Coull, J.; et al. Solid-Phase Synthesis of Peptide Nucleic Acids. *J. Pept. Sci.* **1995**, *1*, 175−183.
(101) Watson, R. M.; Skorik, Y. A.; Patra, G. K.; Achim, C. Influence of Metal Coordination on the Mismatch Tolerance of Ligand-Modified PNA Duplexes. *J. Am. Chem. Soc.* **2005**, *127*, 14628−14639.
(102) Nielsen, P. E.; Egholm, M. *Peptide Nucleic Acids*; Springer, 1999.
(103) He, W.; Crawford, M. J.; Rapireddy, S.; Madrid, M.; Gil, R. R.; Ly, D. H.; Achim, C. The Structure of a Γ-Modified Peptide Nucleic Acid Duplex. *Mol. Biosyst.* **2010**, *6*, 1619−1629.
(104) Dragulescu-Andrasi, A.; Rapireddy, S.; Frezza, B. M.; Gayathri, C.; Gil, R. R.; Ly, D. H. A Simple Γ-Backbone Modification Preorganizes Peptide Nucleic Acid into a Helical Structure. *J. Am. Chem. Soc.* **2006**, *128*, 10258−10267.
(105) Wittung, P.; Eriksson, M.; Lyng, R.; Nielsen, P. E.; Norden, B. Induced Chirality in PNA-PNA Duplexes. *J. Am. Chem. Soc.* **1995**, *117*, 10167−10173.
(106) Peisach, J.; Blumberg, W. E. Structural Implications Derived from the Analysis of Electron Paramagnetic Resonance Spectra of Natural and Artificial Copper Proteins. *Arch. Biochem. Biophys.* **1974**, *165*, 691−708.
(107) Franzini, R. M.; Watson, R. M.; Patra, G. K.; Breece, R. M.; Tierney, D. L.; Hendrich, M. P.; Achim, C. Metal Binding to Bipyridine-Modified PNA. *Inorg. Chem.* **2006**, *45*, 9798−9811.
(108) Kanamaru, F.; Ogawa, K.; Nitta, I. The Crystal Structures of Metal 8-Hydroxyquinolinate. I. Copper 8-Hydroxyquinolinate. *Bull. Chem. Soc. Jpn.* **1963**, *36*, 422−427.
(109) Etaiw, S. E.-d. H.; El-bendary, M. M. Crystal Structure, Characterization and Catalytic Activities of Cu(II) Coordination Complexes with 8-Hydroxyquinoline and Pyrazine-2-Carboxylic Acid. *Appl. Organomet. Chem.* **2018**, *32*, No. e4213.
(110) Gamble Jarvi, A.; Ranguelova, K.; Ghosh, S.; Weber, R. T.; Saxena, S. On the Use of Q-Band Double Electron−Electron Resonance to Resolve the Relative Orientations of Two Double Histidine-Bound Cu2+ Ions in a Protein. *J. Phys. Chem. B* **2018**, *122*, 10669−10677.
(111) Engelhard, D. M.; Meyer, A.; Berndhäuser, A.; Schiemann, O.; Clever, G. H. Di-Copper(Ii) DNA G-Quadruplexes as EPR Distance Rulers. *Chem. Commun.* **2018**, *54*, 7455−7458.
(112) Denysenkov, V. P.; Prisner, T. F.; Stubbe, J.; Bennati, M. High-Field Pulsed Electron−Electron Double Resonance Spectroscopy to Determine the Orientation of the Tyrosyl Radicals in Ribonucleotide Reductase. *Proc. Natl. Acad. Sci. U.S.A.* **2006**, *103*, 13386−13390.
(113) Schiemann, O.; Cekan, P.; Margraf, D.; Prisner, T. F.; Sigurdsson, S. T. Relative Orientation of Rigid Nitroxides by Peldor: Beyond Distance Measurements in Nucleic Acids. *Angew. Chem., Int. Ed.* **2009**, *48*, 3292−3295.
(114) Yang, Z.; Kise, D.; Saxena, S. An Approach Towards the Measurement of Nanometer Range Distances Based on Cu2+ Ions and ESR. *J. Phys. Chem. B* **2010**, *114*, 6165−6174.
(115) Bowen, A. M.; Jones, M. W.; Lovett, J. E.; Gaule, T. G.; McPherson, M. J.; Dilworth, J. R.; Timmel, C. R.; Harmer, J. R. Exploiting Orientation-Selective Deer: Determining Molecular Structure in Systems Containing Cu(Ii) Centres. *Phys. Chem. Chem. Phys.* **2016**, *18*, 5981−5994.
(116) Abé, C.; Klose, D.; Dietrich, F.; Ziegler, W. H.; Polyhach, Y.; Jeschke, G.; Steinhoff, H.-J. Orientation Selective Deer Measurements on Vinculin Tail at X-Band Frequencies Reveal Spin Label Orientations. *J. Magn. Reson.* **2012**, *216*, 53−61.
(117) Bode, B. E.; Plackmeyer, J.; Prisner, T. F.; Schiemann, O. Peldor Measurements on a Nitroxide-Labeled Cu(II) Porphyrin: Orientation Selection, Spin-Density Distribution, and Conformational Flexibility. *J. Phys. Chem. A* **2008**, *112*, 5064−5073.
(118) Tkach, I.; Pornsuwan, S.; Höbartner, C.; Wachowius, F.; Sigurdsson, S. T.; Baranova, T. Y.; Diederichsen, U.; Sicoli, G.; Bennati, M. Orientation Selection in Distance Measurements between Nitroxide Spin Labels at 94 Ghz EPR with Variable Dual Frequency Irradiation. *Phys. Chem. Chem. Phys.* **2013**, *15*, 3433−3437.
(119) Denysenkov, V. P.; Biglino, D.; Lubitz, W.; Prisner, T. F.; Bennati, M. Structure of the Tyrosyl Biradical in Mouse R2 Ribonucleotide Reductase from High-Field Peldor. *Angew. Chem., Int. Ed.* **2008**, *47*, 1224−1227.
(120) Marko, A.; Prisner, T. F. An Algorithm to Analyze Peldor Data of Rigid Spin Label Pairs. *Phys. Chem. Chem. Phys.* **2013**, *15*, 619−627.
(121) Marko, A.; Margraf, D.; Cekan, P.; Sigurdsson, S. T.; Schiemann, O.; Prisner, T. F. Analytical Method to Determine the Orientation of Rigid Spin Labels in DNA. *Phys. Rev. E* **2010**, *81*, No. 021911.
(122) Lovett, J. E.; Bowen, A. M.; Timmel, C. R.; Jones, M. W.; Dilworth, J. R.; Caprotti, D.; Bell, S. G.; Wong, L. L.; Harmer, J. Structural Information from Orientationally Selective Deer Spectroscopy. *Phys. Chem. Chem. Phys.* **2009**, *11*, 6840−6848.
(123) Marko, A.; Denysenkov, V.; Margraf, D.; Cekan, P.; Schiemann, O.; Sigurdsson, S. T.; Prisner, T. F. Conformational Flexibility of DNA. *J. Am. Chem. Soc.* **2011**, *133*, 13375−13379.
(124) Yang, Z.; Ji, M.; Saxena, S. Practical Aspects of Copper Ion-Based Double Electron Electron Resonance Distance Measurements. *Appl. Magn. Reson.* **2010**, *39*, 487−500.
(125) Ji, M.; Ruthstein, S.; Saxena, S. Paramagnetic Metal Ions in Pulsed ESR Distance Distribution Measurements. *Acc. Chem. Res.* **2014**, *47*, 688−695.
(126) Dickerson, R. E. Definitions and Nomenclature of Nucleic Acid Structure Parameters. *J. Biomol. Struct. Dyn.* **1989**, *6*, 627−634.
(127) Li, S.; Olson, W. K.; Lu, X.-J. Web 3dna 2.0 for the Analysis, Visualization, and Modeling of 3D Nucleic Acid Structures. *Nucleic Acids Res.* **2019**, *47*, W26−W34.

https://dx.doi.org/10.1021/acs.jpcb.0c05509
J. Phys. Chem. B XXXX, XXX, XXX−XXX